INORGANIC CHEMISTRY
FRONTIERS

RESEARCH ARTICLE

View Article Online
View Journal

Cite this: DOI: 10.1039/d5qi01345c

Interfacial regulation for constructing a robust grapevine-like conductive network within a silicon-based anode for high-performance lithium-ion batteries

Chuhan Zhou, Xiangxiang Wang, Kun Wang, Siying Li, Xingyu Sun, Zhouying Wu, Lina Wang, Chengdu Liang and Min Ling *

Silicon-based anodes hold significant promise for the development of next-generation lithium-ion batteries, attracting global attention due to their high theoretical capacity. However, silicon-based anodes undergo substantial volume expansion and high mechanical stress, which could disrupt conventional Super P (SP)-based conductive networks within the electrode, leading to capacity degradation. Furthermore, SP tends to agglomerate in aqueous solvents, which limits its conductive effectiveness. To address these challenges, we developed a composite material based on carbonized bacterial cellulose (CBC) and sodium carboxymethyl cellulose (CMC). This novel material enables uniform dispersion of SP, thereby constructing a robust grapevine-like structured conductive network. This network mimics the structure of a vine with grape clusters. The "grape clusters" consist of uniformly dispersed SP particles that serve as highly efficient conductive nodes. The "vine" structure, acting as a flexible and robust framework, enhances the mechanical properties of the electrode, thereby maintaining the structural integrity of the electrode during cycling. Consequently, the SiO_x@CBC–CMC electrode exhibits impressive cycling and rate performances. Specifically, the electrode displays almost no capacity decay after 300 cycles at 0.5C, and its average discharge specific capacity is as high as 535 mAh g^{-1} at 2C. This work designed a novel conductive enhancement network, offering a promising pathway to overcome the conductivity limitations of silicon-based anodes.

Received 20th June 2025,
Accepted 12th August 2025

DOI: 10.1039/d5qi01345c

rsc.li/frontiers-inorganic

1. Introduction

Given the growing demand for higher energy density, extended cycling lifespan, and enhanced safety,[1–3] silicon-based anodes have become a global focus.[4] However, the large volume variations cause a compressive stress as high as 0.5 GPa and a tensile stress reaching up to 2 GPa,[5] both of which could break the traditional Super P (SP)-based conductive network.[6–9] Due to the high surface area of SP (>60 m^2 g^{-1}), the strong van der Waals forces between SP particles readily induce their aggregation, making them difficult to disperse uniformly.[10] Moreover, the compatibility of SP is particularly problematic in aqueous solvents, where agglomeration is more pronounced.[11,12] The breakage of silicon-based active materials and aggregation of SP within the electrode result in an unstable solid electrolyte interphase (SEI) layer and a defective conductive network, limiting the commercial application of silicon-based anodes.[13]

To construct a more efficient and stable conductive network within the electrode, researchers have explored several approaches: (1) conductive agents with higher spatial dimensionality: high-dimensional conductive agents can significantly improve the performance of the conductive network.[14,15] For instance, the volume electrical conductivity of carbon nanotubes (one-dimensional, 1D)[14,16,17] and graphene (two-dimensional, 2D)[18] is approximately 100 times higher than that of SP (zero-dimensional, 0D). However, these high-dimensional conductive agents come with higher costs and significantly greater challenges in achieving uniform dispersion.[19] (2) Modification of conductive agents: various modification strategies have been explored to enhance the performance of conductive properties. Cao *et al.* reported a surface modification method to increase the specific surface area of the conductive agent using H_2SO_4, thereby achieving superior cycling and rate performances.[20] Marinaro *et al.* loaded copper nanoparticles onto SP to serve as a conductive additive for lithium-ion batteries. Anodes using the Cu/SP additive exhibi-

Zhejiang Provincial Key Laboratory of Advanced Chemical Engineering Manufacture Technology, College of Chemical and Biological Engineering, Zhejiang University, Hangzhou 310027, Zhejiang, China. E-mail: minling@zju.edu.cn, 22328148@zju.edu.cn

ted excellent cycling stability at temperatures as low as −30 °C.[21] However, the modification of SP often involves complex procedures, higher costs, and the introduction of impurities, which limit its practical application. (3) Modification of silicon-based materials to stabilize conductive networks: Manj *et al.* engineered carbon-coated SiNPs (SiC) and MXene-based hybrid structured active materials to effectively suppress volume expansion and stabilize conductive networks.[22] Li *et al.* controlled the crystallinity of SiO_x to stabilize the electrode architecture, thereby maintaining electrical contact between active materials.[23] However, the modification of active materials faces multiple challenges including cost, environmental impact, and processing complexities.

Herein, we developed a composite material based on carbonized bacterial cellulose and carboxymethyl cellulose sodium (CBC–CMC) through dispersing and hydrothermally carbonizing (HTC) bacterial cellulose (BC). CBC–CMC enables uniform dispersion of SP, which facilitates the formation of a robust grapevine-like conductive network structure in SiO_x@CBC–CMC electrodes. This structure with multiple conductive pathways could construct a highly efficient and stable conductive network, thereby maintaining electrical contact during lithiation/delithiation.[19,24,25] Under the same applied voltage, the average current of the SiO_x@CBC–CMC electrode (35.1 nA) is 4.4 times higher than that of the SiO_x@PAA electrode (8.0 nA). Based on hierarchical structure research[26] and fiber-reinforced material theory,[27] the "vine" network[28] formed by CBC–CMC, which possesses a high aspect ratio and high mechanical strength,[29] can effectively enhance the mechanical properties of the electrode. The DMT modulus of the SiO_x@CBC–CMC electrode increased by 58.4% and the volume expansion rate reduced by 70.9%. Additionally, CBC–CMC possesses a porous structure and is rich in oxygen-containing functional groups,[30,31] exhibiting better compatibility with both SP and active materials SiO_x. Scheme 1 vividly depicts the advantages of CBC–CMC: (a) forming a highly efficient conductive network with a grape-like chain structure by guiding the uniform distribution of SP; (b) enhancing the mechanical properties of the electrode due to the "vine" structure; and (c) exhibiting better compatibility with SiO_x through initiating hydrogen bonding. This innovative application of bacterial cellulose provides a micro-SiO_x electrode with an efficient conductive network and impressive mechanical properties. The SiO_x@CBC–CMC electrode demonstrates better cycling performance and rate capability compared to the SiO_x@PAA electrode. Simultaneously, the high-loading SiO_x@CBC–CMC electrode (2 mg cm^{-2}) maintains a capacity of 1031 mAh g^{-1} after 100 cycles at 0.2C, with a capacity retention of 88.6%.

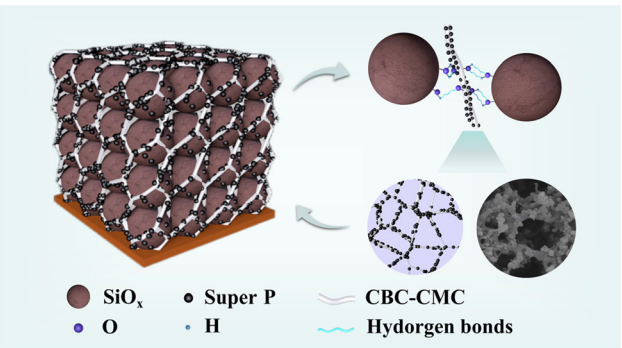

Scheme 1 Schematic illustration of the SiO_x anode with SP and CBC–CMC.

2. Experimental

2.1. Materials

Bacterial cellulose was purchased from Guilin Qihong Technology Co., Ltd. The bacterial cellulose dispersion has a solid content of 0.8%, with bacterial cellulose fibers measuring 50–100 nm in diameter and approximately 20 μm in length. Poly(acrylic acid) (PAA, MW = 1 250 000) was obtained from Sigma-Aldrich. The SiO_x material was supplied by Wynca Chemical Group Co., Ltd. Super P (SP) was procured from Guangdong Canrd New Energy Technology Co., Ltd. Carboxymethyl cellulose sodium (CMC) was obtained from Aladdin Biochemical Technology Co., Ltd.

2.2. Treatment of bacterial cellulose

The BC aqueous dispersion (0.8 wt% solid content) was sealed in an autoclave and carbonized at 200 °C for 900 minutes under self-generated pressure. The resulting carbonized bacterial cellulose was named carbonized bacterial cellulose (CBC). Furthermore, carboxymethyl cellulose sodium (CMC) was added to the BC dispersion at a 1 : 1 mass ratio (BC : CMC). The mixture was stirred at 500 rpm for 10 min at room temperature to obtain a homogeneous solution with a total solid content of 0.8 wt%. The mixed solution was then placed into an autoclave reactor and heated at 200 °C for 900 minutes. The resulting material was named carbonized bacterial cellulose–carboxymethyl cellulose sodium (CBC–CMC), exhibiting a three-dimensional porous structure.

2.3. Preparation of electrodes

The SiO_x@CBC–CMC electrode was prepared through a series of steps. CBC–CMC was separately dispersed in a 2 wt% polyacrylic acid (PAA) aqueous solution at a fixed PAA-to-CBC–CMC weight ratio of 9 : 1, followed by stirring at 2000 rpm for 5 min. The electrode slurry was prepared by mixing 80 wt% SiO_x, 10 wt% Super P conductive carbon, and 10 wt% PAA–CBC–CMC. (The described material addition sequence represents just one viable processing route, as alternative addition orders can also be effectively implemented.) The slurry was homogenized using a planetary mixer at 2000 rpm for 15 min, then coated onto copper foil current collectors and dried under dynamic vacuum at 100 °C for 12 h. The fabrication process of the SiO_x@PAA, SiO_x@CBC, and SiO_x@BC electrodes was identical to that of the SiO_x@CBC–CMC electrode. Two sets of electrodes were prepared with SiO_x areal mass loadings of ~1.0 mg cm^{-2} and ~2.0 mg cm^{-2}.

2.4. Cell assembly and electrochemical measurements

For the half-cell evaluation, 2025-type coin cells were assembled using a SiO_x electrode, a lithium metal counter electrode, and a Celgard 2325 membrane separator. Galvanostatic charge–discharge cycling tests were performed using a LAND battery cycler within a voltage range of 0.005–1.5 V. Galvanostatic intermittent titration technique (GITT) tests were performed using the LAND battery cycler within a voltage range of 0.005–1.5 V. The tests employed a pulse period of 10 minutes and a relaxation period of 30 minutes. Electrochemical impedance spectroscopy (EIS) measurements were carried out using a CHI760E instrument over a frequency range of 0.01 Hz to 100 kHz, with an amplitude of 5 mV. All experiments were conducted at an ambient temperature of 25 °C.

2.5. Materials characterization

The microstructures of the aforementioned materials were characterized using a field-emission scanning electron microscope (FE-SEM, Hitachi SU-8010) and a high-resolution transmission electron microscope (HR-TEM, Hitachi HT-7700). Energy dispersive spectroscopy (EDS) was used to analyze the elemental distribution. Fourier-transform infrared spectrometry (FTIR) measurements were conducted using a Nicolet iS50 spectrophotometer within a wavenumber range of 4000 to 400 cm^{-1}. X-ray photoelectron spectroscopy (XPS) was performed with a Thermo Scientific K-Alpha instrument, utilizing an Al Kα radiation source. Raman spectroscopy tests on various bacterial cellulose samples were conducted using a spectrometer (Horiba LabRAM HR Evolution), in the range of 50–4000 cm^{-1}. Zeta potential measurements were conducted using a zeta potential analyzer (Malvern Zetasizer Nano-ZS). The contact angles between materials were measured using the sessile drop method with a video-based, contact angle measuring device (Dataphysics OCA 20). PeakForce QNM (Quantitative Nanomechanical Mapping) atomic force microscopy (AFM) experiments were performed using a Bruker Dimension Icon instrument to evaluate the adhesion, DMT modulus, and height sensor of various electrodes (peak force frequency was 2000 Hz, used RTESPA-525). The conductivity of various electrodes was tested using PeakForce TUNA (tunneling atomic force microscopy) experiments with an applied voltage of 100 mV. The resistivity of various electrode slurries was tested using a slurry resistivity meter (BSR2300) from IEST (Initial Energy Science & Technology (Xiamen) Co., Ltd).

3. Results and discussion

3.1. Bacterial cellulose constructs a stable conductive network

The highly efficient grapevine-like conductive network was achieved through the incorporation of BC and CMC, and the morphology evolution during the incorporation was recorded as shown in Fig. 1. In Fig. 1a–f, untreated BC exhibits a fibrous morphology with a high aspect ratio, featuring diameters of 50–100 nm and lengths of approximately 20 μm. Multiple fibers form a uniform network structure. The fibrous morphology of carbonized bacterial cellulose (CBC) is partially disrupted, with larger carbon dots appearing on the fiber network, which affects the material's uniformity. By combining steric hindrance and electrostatic adsorption, CMC effectively disperses BC,[32] and subsequent hydrothermal carbonization of the dispersion yields CBC–CMC (Fig. S1). CBC–CMC largely retains the fibrous morphology of BC, with small carbon particles formed from the carbonization of CMC coating (Fig. S2) and adhering to the bacterial cellulose, resulting in a uniform network structure. When the BC : SP ratio is 1 : 10 (Fig. S3), SP is uniformly distributed on BC, constructing an efficient conductive network (Fig. 1g). BC possesses an extremely high specific surface area as a nanoscale material, which enhances van der Waals force with other materials.[33] This strengthens the adsorption of other particles and facilitates the formation of a relatively stable structure.[34] Furthermore, CBC–CMC enables more effective dispersion of SP within the fibrous network, forming a conductive network with a grape-like chain structure (Fig. 1h). CBC–CMC preserves the intrinsic nanofiber architecture while demonstrating enhanced compatibility with SP, enabling the formation of a grapevine-like conductive network comprising branched structures and nano-sized conductive carbon particles. Notably, the grapevine-like network structures formed by SP under the guidance of CBC–CMC are observed in the electrodes both before and after cycling (Fig. S4).

To investigate the effect of CBC–CMC addition on the dispersion uniformity of electrode materials, comprehensive material characterization studies were conducted, including Raman spectroscopy, contact angle measurements, Fourier-transform infrared spectroscopy (FTIR), and zeta potential analysis. As shown in Fig. 2a, Raman spectroscopy revealed that the I_D/I_G ratios for CBC–CMC (Fig. 2b) and CBC (Fig. 2d) were 1.03 and 1.46, respectively. The higher the I_D/I_G value of a material, the more disordered its microstructure and the lower its degree of graphitization.[35,36] This indicates that CBC–CMC has a higher degree of graphitization. According to the principle of like dissolves like,[37,38] CBC–CMC exhibits better compatibility with SP. Moreover, the enhanced graphitization degree of CBC–CMC contributes to improved intrinsic conductivity of the material.[39] T. Young proposes that a smaller contact angle correlates with a higher solid–liquid interfacial energy, indicating enhanced compatibility between the two materials.[40] As shown in Fig. S5, the contact angles of BC, CBC, and CBC–CMC (water solvent) with SP were 138.7°, 117.5°, and 93.8°, respectively. Both tests demonstrate that the compatibility of BC with SP improves after hydrothermal carbonization, and CBC–CMC exhibits better compatibility with SP than CBC.

Additionally, CBC–CMC also exhibits excellent compatibility with SiO_x and PAA, which helps maintain the stability of the conductive network and enhances the overall performance of the electrode. FTIR results confirmed that the chemical functional groups of BC and CBC–CMC remain largely

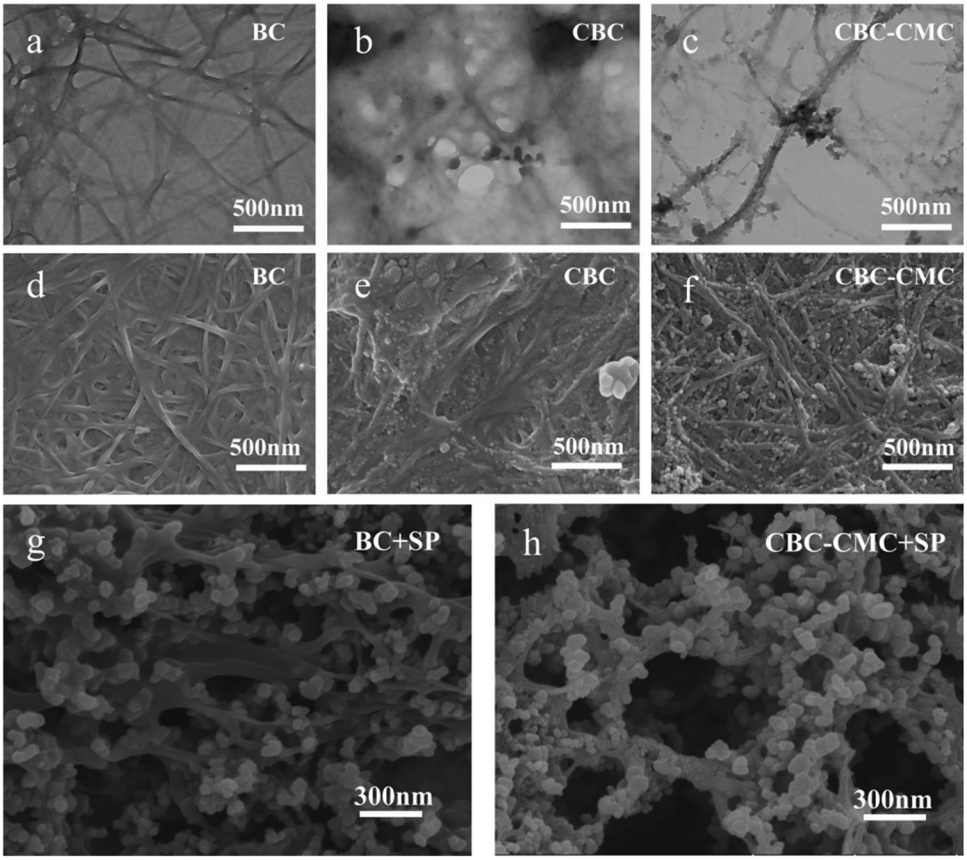

Fig. 1 (a–c) TEM images and (d–f) SEM images of BC, CBC and CBC–CMC. (g) SEM images of BC and SP (BC : SP = 1 : 10). (h) SEM images of CBC–CMC and SP (CBC–CMC : SP = 1 : 10).

unchanged, with CBC–CMC retaining a significant number of oxygen-containing groups (Fig. S6). CBC–CMC could form hydrogen bonding with PAA (Fig. S7) and SiO_x (Fig. S8), indicating good compatibility with SiO_x and the binder PAA.[41] The absolute values of the zeta potentials in both the SP dispersion and electrode slurry were higher than those without CBC–CMC (Fig. 2c). A higher absolute zeta potential indicates greater system stability, demonstrating that CBC–CMC promotes the stable dispersion of the electrode slurry. Sedimentation tests of the different slurries provide further evidence for this conclusion (Fig. S9 and S10). Furthermore, contact angle measurements between the electrodes and the electrolyte demonstrate that the SiO_x@CBC–CMC electrode also possesses favorable interfacial compatibility with the electrolyte (Fig. S11). In summary, CBC–CMC exhibits superior compatibility with SP and demonstrates excellent interfacial affinity with both SiO_x and PAA, contributing to enhanced slurry stability and homogeneous electrode formulation.

3.2. Conductive networks and conductivity

To investigate the effects of BC and CBC–CMC on the conductive network and electronic conductivity of the electrode, PeakForce TUNA (tunneling atomic force microscopy) and the resistivity and conductivity tests were performed on different SiO_x electrodes. A bias of 100 mV was applied to each sample, and the resulting response current was used to assess the electrode's conductivity and to map the distribution of conductive materials. Fig. 3a reveals that the current distribution of the SiO_x@PAA electrode is highly non-uniform, attributed to poor dispersion and agglomeration of SP within the electrode. Fig. 3b shows that the current distribution of the SiO_x@BC electrode is improved, indicating that BC promotes a more uniform distribution of SP in the electrode. Nevertheless, the average current of the SiO_x@BC electrode decreases due to the inherently low conductivity of BC. Fig. 3c demonstrates that the SiO_x@CBC–CMC electrode exhibits a highly uniform current distribution, along with a significant increase in average current compared to the SiO_x@PAA electrode. This indicates that CBC–CMC effectively guides the uniform distribution of SP within the electrode while enhancing the electronic conductivity of the electrode. Specifically, the average currents of the SiO_x@PAA, SiO_x@BC, and SiO_x@CBC–CMC electrodes were 8.0 nA, 4.3 nA, and 35.1 nA, respectively (Fig. 3d).

Additionally, the resistivity and conductivity of different slurries and electrode solid powders were measured. As shown in Fig. 3e and f, the conductivity of the SiO_x@BC slurry decreased compared to that of SiO_x@PAA. Although BC

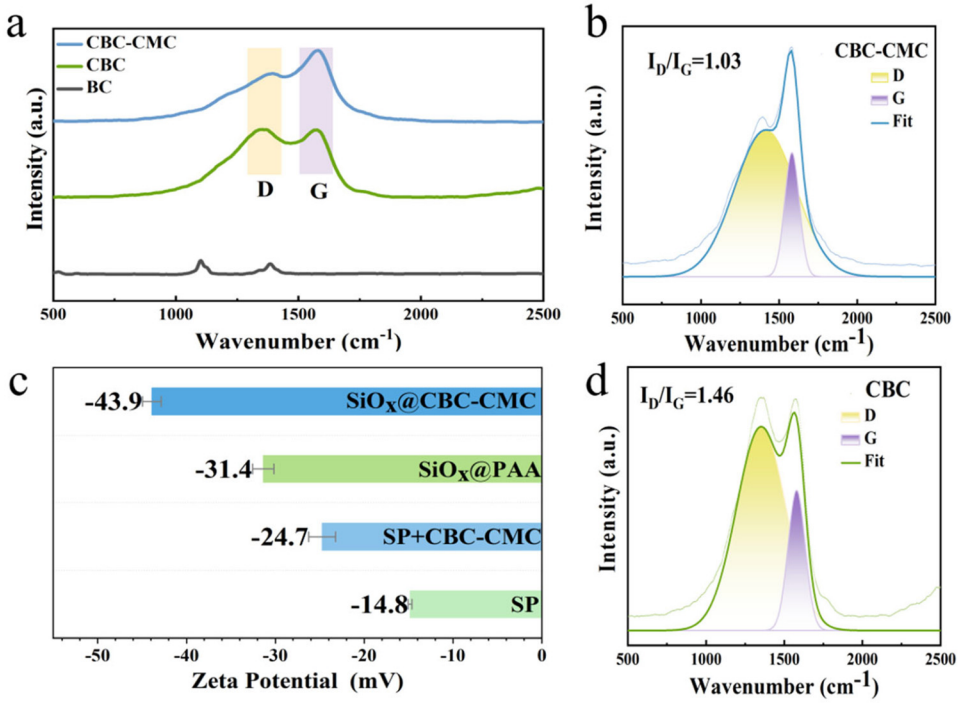

Fig. 2 (a) Raman spectra of different bacterial cellulose materials. (b) Raman spectra of CBC–CMC. (c) Zeta potentials of the SP dispersion and electrode slurry before and after the addition of CBC–CMC. (d) Raman spectra of CMC.

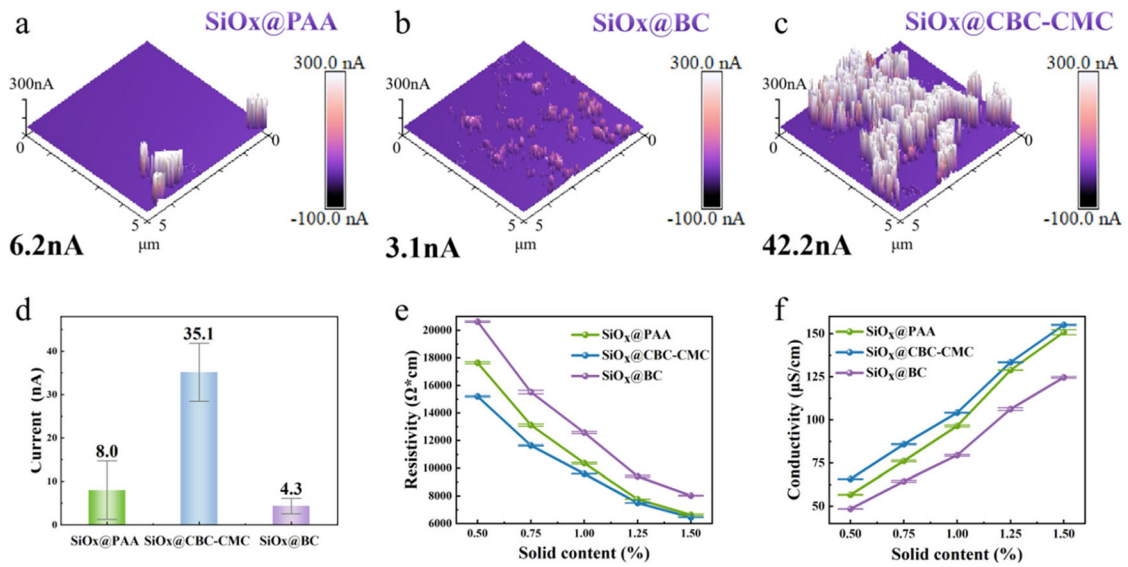

Fig. 3 PeakForce TUNA images of the (a) SiO_x@PAA electrode, (b) SiO_x@BC electrode and (c) SiO_x@CBC–CMC electrode. (d) The average currents of different SiO_x electrodes. The (e) resistivity and (f) conductivity of different electrode slurries.

improves the dispersion of SP in the slurry, it reduces the slurry conductivity due to its high resistivity. In contrast, the conductivity of the SiO_x@CBC–CMC slurry increased compared to that of SiO_x@PAA, indicating that CBC–CMC enhances the electronic conductivity of the electrode slurry. The conductivity measurements of the solid powders were consistent with those of the slurries (Fig. S12). These results further macroscopically demonstrate that CBC–CMC not only efficiently guides the uniform distribution of SP but also positively impacts the electronic conductivity of the electrode. Overall, while BC enables uniform distribution of SP within the electrode, it imposes certain limitations on electronic

conductivity. In contrast, the CBC–CMC composite not only achieves more efficient and homogeneous SP dispersion but also significantly enhances the conductivity of the electrode.

3.3. Analysis of mechanical properties, adhesion and surface roughness

To investigate the effects of BC and CBC–CMC incorporation on the mechanical properties, adhesion strength, and surface roughness of electrodes, a comprehensive evaluation was conducted using an atomic force microscope (AFM), combined with the Derjaguin–Muller–Toporov (DMT) model, 180° peel tests and folding tests. The average DMT modulus of SiO_x@PAA is 5.91 GPa, while the average DMT modulus of SiO_x@BC and SiO_x@CBC–CMC is 9.24 GPa and 9.22 GPa, respectively (Fig. 4a–c). Multiple parallel experiments (Fig. S13) confirmed that the SiO_x@CBC–CMC electrode (10.28 GPa) exhibits a 58.4% higher average DMT modulus compared to the SiO_x@PAA electrode (6.49 GPa), demonstrating significantly enhanced mechanical robustness. The incorporation of BC and CBC–CMC significantly enhances the overall DMT modulus of the electrode, enabling it to withstand the substantial mechanical stresses induced by rapid volume changes under high current densities.

As shown in Fig. 4e–g, the average adhesion of the SiO_x@BC (64.5 nN) and SiO_x@CBC–CMC electrodes (61.7 nN) is higher than that of the SiO_x@PAA electrode (47.4 nN). The added BC improves the overall adhesion of the electrode, which is conducive to reducing the flaking of active materials and SP from the electrode. Furthermore, 180° peel test results also demonstrate that the incorporation of CBC–CMC significantly enhances the adhesive strength of the electrode (Fig. S14), and the electrode maintained structural integrity after the peel tests (Fig. S15). The results of the folding tests corroborate this conclusion (Fig. S16). The elevated DMT modulus and peel strength stem from synergistic chemical and physical effects. Chemically, carbonized CBC–CMC retains abundant oxygenated groups (Fig. S6) that form H-bonds with PAA (Fig. S7) and SiO_x (Fig. S8), and exhibits "like-dissolves-like" compatibility with SP (Fig. S5, Fig. 2), generating robust interfacial cohesion. Physically, high-aspect-ratio CBC–CMC nanofibers create a stiff, continuous network that redistributes shear stresses during peeling and establishes mechanical bridging within the electrode (Fig. S4).

Notably, the root-mean-square roughness (rq) of the SiO_x@CBC–CMC electrode is 16.6 nm, which is smaller than the rq of the SiO_x@PAA (31.8 nm) and SiO_x@BC (25.7 nm) electrodes (Fig. 4g–i). CBC–CMC reduces the agglomeration of SP due to the good compatibility of CBC–CMC with the conductive agent and the active material, resulting in a more uniform distribution of SP within the electrode. This improve-

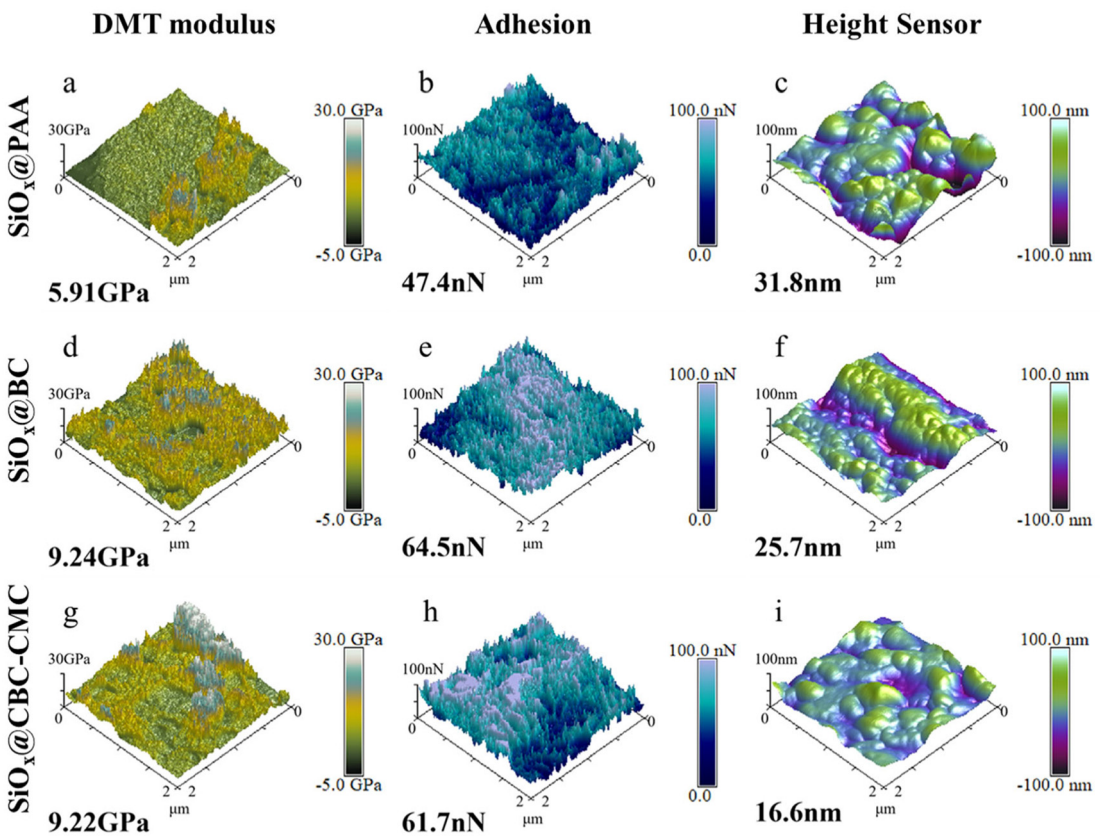

Fig. 4 (a) DMT modulus, (b) adhesion and (c) height sensor mappings of the SiO_x@PAA electrode. (d) DMT modulus, (e) adhesion and (f) height sensor mappings of the SiO_x@BC electrode. (g) DMT modulus, (h) adhesion and (i) height sensor mappings of the SiO_x@CBC–CMC electrode.

ment mitigates the roughness of the electrode surface to some extent, leading to a smoother and flatter surface of the electrode sheet, thereby enhancing the overall performance of the electrode. BC and CBC–CMC materials within electrodes enhance the mechanical strength of the electrode through fiber reinforcement (56% improvement), enabling the SiO_x electrode to withstand the significant mechanical stress caused by rapid volume changes under high current densities. These also improve the overall adhesion of the electrode, reducing the flaking of SP and SiO_x during cycling. Additionally, CBC–CMC promotes a more uniform distribution of SP within the electrode, resulting in a smoother and more intact surface of the electrode.

3.4. The electrochemical performance of SiO_x anode-based batteries

The electrochemical performance of different SiO_x electrodes was systematically evaluated through galvanostatic charge–discharge tests to validate the effectiveness of CBC–CMC. To ensure data reliability, three parallel experiments were conducted for each group. The SiO_x@CBC–CMC electrode maintains a high discharge specific capacity of 1288 mAh g^{-1} after 100 cycles at 0.2C, with a capacity retention rate of 91.3%. In comparison, the SiO_x@PAA, SiO_x@BC, and SiO_x@CBC electrodes exhibit lower discharge specific capacities of 958 mAh g^{-1}, 1094 mAh g^{-1}, and 1072 mAh g^{-1}, respectively (Fig. 5a). Notably, in higher loading tests (2 mg cm^{-2}), SiO_x@CBC–CMC still maintained a superior capacity (1031 mAh g^{-1}) and cycling stability (88.6% capacity retention), attributed to the formation of a robust conductive network preventing the formation of "isolated SiO_x" (Fig. 5b).

To gain further insights into the performance of CBC–CMC, extended cycling tests were conducted. Under restricted capacity (600 mAh g^{-1}) at 1 A g^{-1} (to avoid the excessive expansion of SiO_x), the SiO_x@CBC–CMC electrode sustained over 500 cycles, far exceeding SiO_x@PAA (260 cycles), and maintained 986 mAh g^{-1} over 300 cycles at 0.5C, *versus* 269 mAh g^{-1} for SiO_x@PAA (Fig. 5c and d), with smaller error bars indicating improved reproducibility. Charge–discharge profiles (Fig. 5e and f) further demonstrate the better cycling stability of the SiO_x@CBC–CMC electrode. The results indicate that CBC–CMC can construct an efficient and stable conductive network within the electrode, thereby achieving enhanced cycling stability during long-term cycling.

Notably, according to the initial coulombic efficiency (ICE) shown in Fig. 5g, the SiO_x@CBC–CMC electrodes exhibited

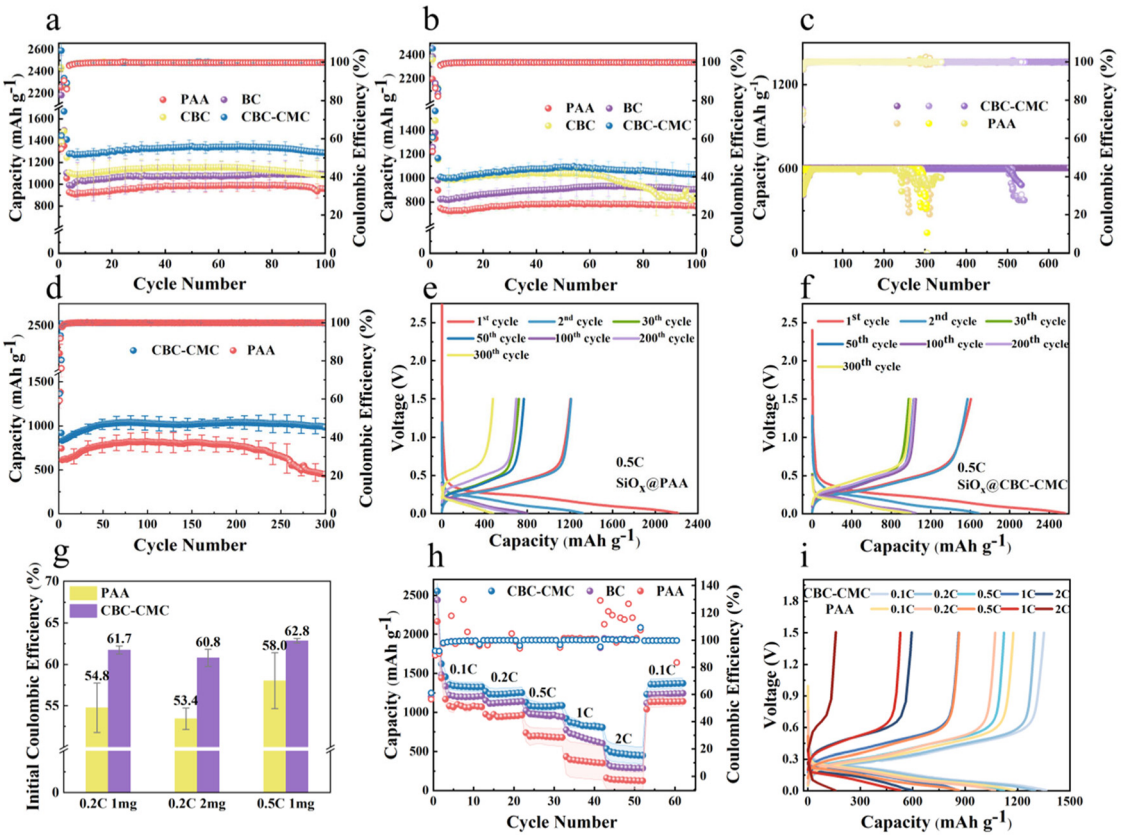

Fig. 5 The cycling performance comparison and the coulombic efficiency of different SiO_x electrodes (a) and different high-loading (2 mg cm^{-2}) SiO_x electrodes (b) at 0.2C (1C = 1600 mA g^{-1}). (c) Cycling performance of different SiO_x electrodes with a limited discharge capacity of 600 mAh g^{-1} at 1 A g^{-1}. (d) The cycling performance of different SiO_x electrodes at 0.5C. The charge–discharge profiles of the SiO_x@PAA electrode (e) and SiO_x@CBC–CMC electrode (f) at 0.5C. (g) The ICE of different electrodes under various cycling conditions. (h) The rate performance of various electrodes. (i) The charge–discharge curves of the different SiO_x electrodes.

higher ICE values under all conditions, suggesting that CBC–CMC can stabilize the electrode/electrolyte interface. Rate capability tests (Fig. 5h) showed that SiO_x@CBC–CMC achieved discharge capacities of 1333 mAh g^{-1}, 1152 mAh g^{-1}, 1021 mAh g^{-1}, 774 mAh g^{-1}, and 535 mAh g^{-1} at 0.1C, 0.2C, 0.5C, 1C, and 2C, respectively, with 93.3% recovery when returned to 0.1C. The charge–discharge curves at different rates (Fig. 5i) demonstrate that the SiO_x@CBC–CMC electrode exhibits significantly superior rate performance and reduced electrochemical and concentration polarization. Overall, the superior cycling and rate performance of SiO_x@CBC–CMC are ascribed to the following: (1) the efficient grapevine-like conductive network formed by uniformly distributed SP enabled by CBC–CMC; (2) enhanced mechanical resilience maintaining structural integrity; and (3) a stabilized electrode/electrolyte interface, reflected by the higher ICE.

3.5. Electrochemical and kinetic analysis

To investigate the underlying reasons for the superior electrochemical performance of the SiO_x@CBC–CMC electrode, electrochemical impedance spectroscopy (EIS) and galvanostatic intermittent titration technique (GITT) tests were performed on both SiO_x@PAA and SiO_x@CBC–CMC electrodes. After electrode activation, the high-frequency semicircle, mid-frequency semicircle, and low-frequency slope correspond to the solid electrolyte interphase (SEI) resistance (R_{SEI}), charge transfer resistance (R_{CT}), and Warburg impedance, respectively (Fig. 6a and b). The R_{SEI}, R_{CT} and lithium-ion diffusion coefficient (D_{Li^+}) values were calculated by fitting the EIS data (Note S1 and Fig. S17), and the results are shown in Fig. 6c–f. The R_{SEI} values of the SiO_x@CBC–CMC electrode after 10, 30 and 90 cycles were 10.9 Ω, 10.9 Ω and 10.1 Ω, respectively. Analogously, the fitted R_{CT} were 6.5 Ω, 7.0 Ω and 7.6 Ω, respectively. The R_{SEI} and R_{CT} values of the SiO_x@CBC–CMC electrode demonstrated remarkable stability. In contrast, the SiO_x@PAA electrode exhibited higher R_{SEI} and R_{CT} values during cycling and significant increases after 90 cycles (R_{SEI} was 59.2 Ω, R_{CT} was 13.8 Ω). This could be attributed to the fact that the network structure of CBC–CMC effectively mitigates volume expansion in the electrode and stabilizes the SEI layer. Furthermore, CBC–CMC enhances electrical contact between active materials and improves charge transfer efficiency. After 90 cycles, the D_{Li^+} values for the SiO_x@CBC–CMC and SiO_x@PAA electrodes were 11.44×10^{-13} cm^2 s^{-1} and 1.97×10^{-13} cm^2 s^{-1}, respectively. These results indicate that CBC–CMC enables the maintenance of electrode structural

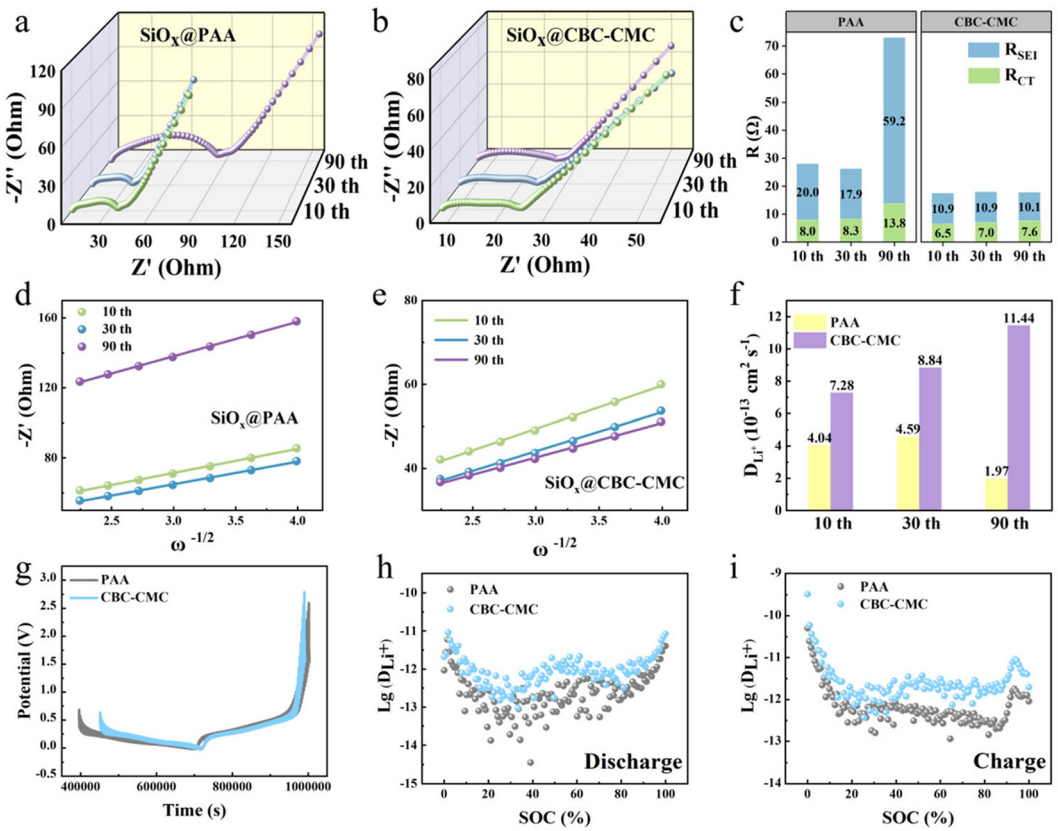

Fig. 6 EIS plots of (a) the SiO_x@PAA electrode and (b) the SiO_x@CBC–CMC electrode after 10, 30 and 90 cycles. (c) R_{CT} and R_{SEI} of different SiO_x electrodes after 10, 30 and 90 cycles. The Warburg impedance plots of (d) the SiO_x@PAA electrode and (e) the SiO_x@CBC–CMC electrode. (f) Comparison of diffusion coefficients calculated from EIS measurements for various SiO_x electrodes. (g) GITT curves of different SiO_x electrodes. D_{Li^+} of different SOCs during the (h) discharge and (i) charge processes.

integrity and ensures efficient ion contact between electrode materials, thereby enhancing lithium-ion diffusion kinetics within the electrode.

The Li^+ diffusion kinetics of the SiO_x@CBC–CMC electrode were investigated by the GITT test and calculated based on Note S2. As shown in Fig. 6g–i, the SiO_x@CBC–CMC electrode exhibits higher D_{Li^+} values across different SOCs compared to the SiO_x@PAA electrode during both discharge and charge processes. As previously discussed, CBC–CMC not only facilitates the formation of a stable SEI layer on the electrode but also enhances the dispersion of SP within the electrode, increasing the specific surface area of the conductive network. This promotes electrolyte adsorption and improves ionic conductivity. Consequently, the SiO_x@CBC–CMC electrode demonstrates significantly greater D_{Li^+}.

The nanostructure of CBC–CMC can shorten the Li^+ transport distance,[42] reduce polarization, and enhance the contact area with the electrolyte.[43] Moreover, CBC–CMC could

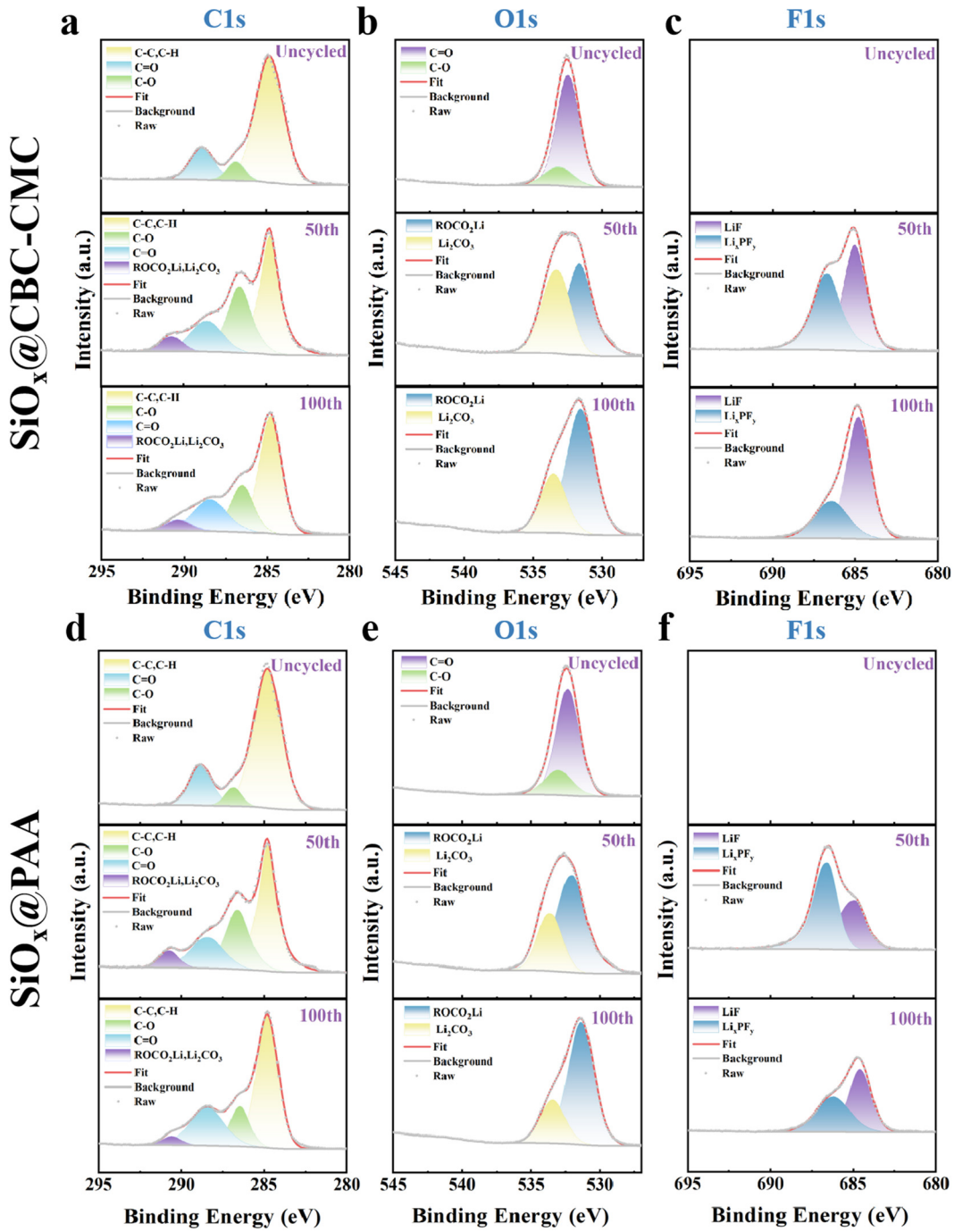

Fig. 7 XPS spectra of the C 1s, O 1s and F 1s peaks of (a–c) the SiO_x@CBC–CMC electrode and (d–f) the SiO_x@PAA electrode before cycling, after 50 cycles, and after 100 cycles.

enhance the mechanical properties of electrodes, preserving structural integrity and safeguarding Li^+ transport pathways.[44] These improve the utilization of active Li^+ and the kinetics of the alloying process. The two nanomaterials, SP and CBC–CMC, construct an efficient and stable conductive network within the electrode, which enhances interfacial current density, promotes charge transfer, and suppresses interfacial polarization.[45] The results from EIS and GITT further confirm that the SiO_x@CBC–CMC electrode possesses a more efficient and stable grapevine-like conductive network, facilitating improved lithium-ion transport efficiency and SEI layer stability, thereby achieving superior electrochemical performance.

3.6. Post-cycling electrode analysis

The role of CBC–CMC in stabilizing the SEI layer was elucidated through XPS analysis. Fig. 7 presents the XPS results of SiO_x@CBC–CMC and SiO_x@PAA electrodes before cycling, after 50 and after 100 cycles at 0.5C. In the C 1s (near 289.1 eV) and O 1s (near 532.9 eV and 531.6 eV) spectra of the different electrodes, peaks corresponding to $ROCO_2Li$ and Li_2CO_3 indicate electrolyte decomposition and then participation in SEI layer formation.[46] After 100 cycles, the peak areas in the C 1s and O 1s spectra of the SiO_x@PAA electrode significantly increase, while the SiO_x@CBC–CMC electrode shows minimal changes. This suggested that CBC–CMC helps restrict the displacement of SP and volume changes of SiO_x, thereby reducing the exposure of fresh electrode surfaces and stabilizing the SEI layer composition. For the F 1s spectrum, the SiO_x@CBC–CMC electrode exhibits a significantly larger LiF peak area (near 684.9 eV)[47] compared to the SiO_x@PAA electrode after 50 cycles. After 100 cycles, the LiF peak area of the SiO_x@PAA electrode decreases markedly, while that of the SiO_x@CBC–CMC electrode remains largely unchanged. The changes in surface atomic composition of different SiO_x electrodes further elucidate that the SiO_x@CBC–CMC electrode formed a stable and LiF-rich SEI layer (Fig. S18). In a previous study, a mechanically robust, LiF-rich SEI layer could accommodate the volume changes of SiO_x, enhance lithium-ion transport, and reduce electrolyte decomposition at the interface, thereby stabilizing the SEI layer composition.[48,49] Li_2CO_3 and $ROCO_2Li$

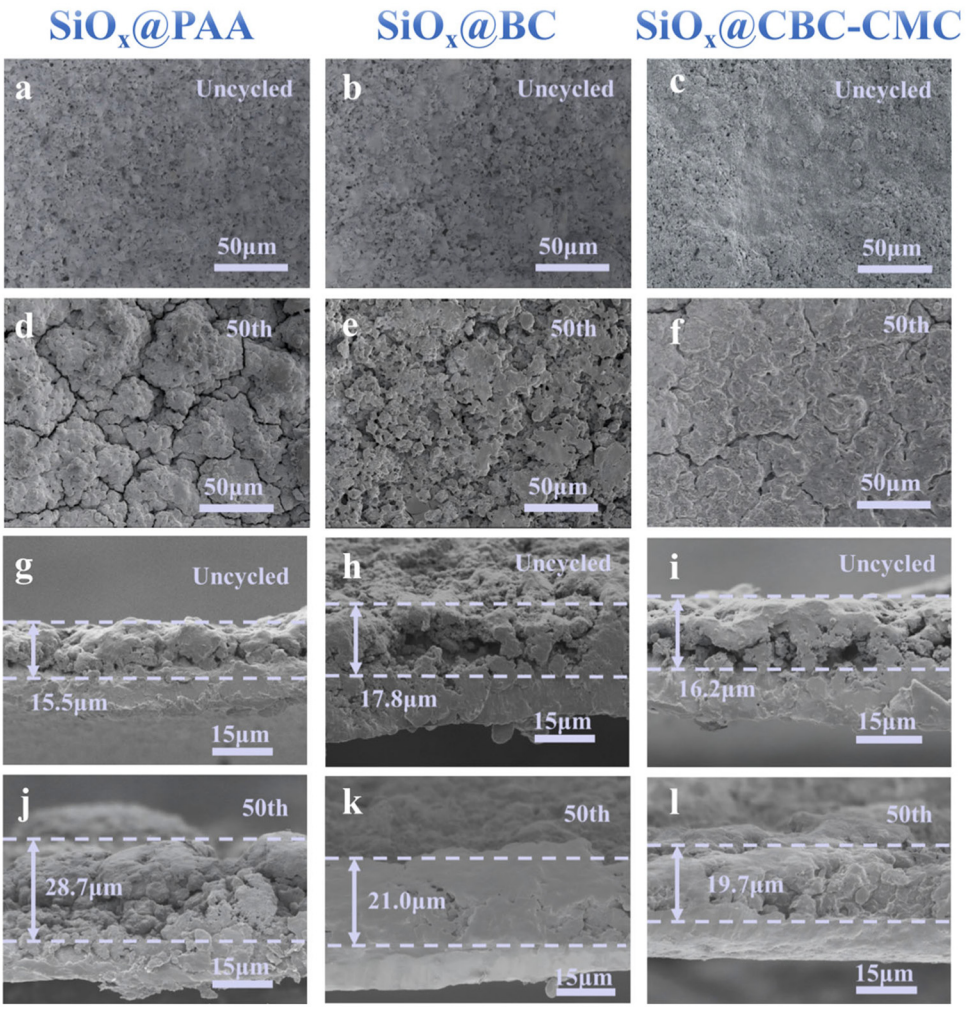

Fig. 8 Top-view SEM images of different electrodes (a–c) before cycling and (d–f) after 50 cycles at 0.5C. Cross-sectional SEM images of different electrodes (g–i) before cycling and (j–l) after 50 cycles at 0.5C.

on the surface of the SiO_x@CBC–CMC electrode are relatively low, while LiF is relatively high, indicating that CBC–CMC can prevent excessive consumption of the electrolyte.

To directly observe the morphology and composition of the SEI layer, we performed TEM and EDS characterization studies on different electrodes. As revealed by TEM characterization (Fig. S19), the SiO_x@CBC–CMC electrode demonstrates a significantly thinner (10–15 nm), more uniform, and densely compacted SEI layer compared to the SiO_x@PAA electrode (20–50 nm). The reduced thickness and enhanced structural homogeneity of the SEI layer suggest improved interfacial stability and more efficient ion transport properties. EDS shows a more uniform and densely distributed F profile in the SiO_x@CBC–CMC electrode (Fig. S20), indicating the formation of a LiF-rich SEI layer. LiF is known to facilitate rapid Li^+ transport due to its high ionic conductivity and electrochemical stability, thereby promoting enhanced Li^+ diffusion kinetics.[50]

To evaluate the role of BC and CBC–CMC in maintaining electrode structural stability, this study employed SEM to observe the surface morphology and cross-sectional thickness changes of different SiO_x electrodes before and after cycling. As shown in Fig. 8a–f, all electrodes exhibited smooth surfaces without any cracks before cycling. After 50 cycles at 0.5C, the SiO_x@PAA electrode showed significant cracking, whereas the SiO_x@BC and SiO_x@CBC–CMC electrodes maintained relatively intact surfaces. Furthermore, the SiO_x@CBC–CMC electrode maintained a more uniform, smooth, and crack-free surface, further demonstrating that CBC–CMC could maintain electrode structural stability during cycling. Fig. 8g–l present cross-sectional SEM images of different SiO_x electrodes before and after cycling. All SiO_x electrodes exhibited similar thicknesses, ranging from 15.5 μm to 17.8 μm before cycling. After cycling, the thickness of the SiO_x@PAA electrode increased by approximately 13 μm (a swelling of 85.2%), and significant cracks were observed in the cross-section. In contrast, the thicknesses of the SiO_x@BC and SiO_x@CBC–CMC electrodes increased by only 18.0% and 21.6%, respectively, with almost no cracks in their cross-sections. Parallel multi-region testing revealed that (Fig. S21) the SiO_x@CBC–CMC electrode (27.8%) exhibits a 70.9% reduction in average volumetric expansion rate compared to the SiO_x@PAA electrode (98.7%). By comparing the surface and cross-sectional SEM images, it is evident that the electrodes with bacterial cellulose maintain structural integrity. These results further corroborate that BC and CBC–CMC can impart high mechanical strength and excellent cycling stability to the electrode, enabling it to accommodate the volume changes of SiO_x during repeated cycling, thereby maintaining electrode structural stability.

4. Conclusions

In conclusion, the introduction of CBC–CMC has successfully established an efficient conductive enhancement network with a grapevine-like structure within the electrode. On the one hand, CBC–CMC effectively facilitates the uniform distribution of SP, expanding the conductive pathways while maintaining the stability of the conductive network during charge–discharge cycles, thereby enhancing the capacity and cycling stability of the electrode. On the other hand, the network structure formed by the high aspect ratio CBC–CMC reinforces the mechanical properties of the electrode, ensuring its structural integrity after prolonged cycling. Additionally, CBC–CMC exhibits better compatibility with SP, SiO_x and PAA, further optimizing the overall electrode performance. Based on these mechanisms, the SiO_x@CBC–CMC electrode exhibits impressive cycling and rate performances, demonstrating a notable capacity retention of 91.3% after 100 cycles and exhibiting an average capacity retention of 93.3% when the current density is restored to 0.1C. This work provides insights into the application of bacterial cellulose in conductive networks, thus inspiring further conductive network engineering in practical LMBs.

Conflicts of interest

The authors declare that they have no known competing financial interests or personal relationships that could have appeared to influence the work reported in this paper.

Data availability

The datasets used and analyzed during the current study are available from the corresponding author upon reasonable request. Supplementary information including experimental and computational details is available. See DOI: **https://doi.org/10.1039/d5qi01345c**.

Acknowledgements

The authors are grateful for the support from the Zhejiang Provincial “Jianbing” and “Lingyan” R&D Programs (No. 2024C01262), the National Natural Science Foundation of China (No. 52172244), the Leading Scientific and Technological Innovation Talents of Zhejiang Province’s “Special Support Plan for High-Level Talents” (No. 2022R52011), and the Zhejiang Provincial “Jianbing” and “Lingyan” R&D Programs (No. 2024C01050). The authors also thank IEST (Initial Energy Science & Technology) (Xiamen) Co., Ltd for the conductivity test of slurries and Shiyanjia Lab (**https://www.shiyanjia.com**) for the XPS and the Raman analysis. The authors also thank Mrs Sudan Shen for her assistance in TEM, Mrs Na Zheng for her assistance in SEM, and Mrs Jing He for her assistance in AFM at the State Key Laboratory of Chemical Engineering in Zhejiang University.

References

1 L. Pan, W. Zhao, L. Zhai, R. Guo, Y. Zhao, X. Wang, C. Wu and Y. Bai, Hierarchical Carbon Interlayer Design as Interfacial Stabilizer and *In situ* Solid-Electrolyte Infiltrate for High-Performance Solid-State Li–S Batteries, *Chem Bio Eng.*, 2024, **1**(4), 340–348.
2 K. Huang, Z. Lu, S. Dai and H. Fei, Recent Progress of Halide Redox Mediators in Lithium–Oxygen Batteries: Functions, Challenges, and Perspectives, *Chem Bio Eng.*, 2024, **1**(9), 737–756.
3 W. Xu, Z. Sun, C. Tang, Z. Cheng, W. Sun, A. Du, Q. Zhang, M. Wu and H. Zhang, Biomimetics-Driven Design of Micron-Sized SiO Composites for High-Performance Lithium-Ion Batteries, *Adv. Funct. Mater.*, 2025, **35**(25), 2422743.
4 M. Li, J. Lu, Z. Chen and K. Amine, 30 Years of Lithium–Ion Batteries, *Adv. Mater.*, 2018, 1800561.
5 Z. Zeng, N. Liu, Q. Zeng, S. W. Lee, W. L. Mao and Y. Cui, In situ measurement of lithiation-induced stress in silicon nanoparticles using micro-Raman spectroscopy, *Nano Energy*, 2016, 105–110.
6 W. Tao, P. Wang, Y. You, K. Park, C.-Y. Wang, Y.-K. Li, F.-F. Cao and S. Xin, Strategies for improving the storage performance of silicon-based anodes in lithium-ion batteries, *Nano Res.*, 2019, **12**(8), 1739–1749.
7 Y. Cui, Silicon anodes, *Nat. Energy*, 2021, **6**(10), 995–996.
8 A. Du, H. Li, X. Chen, Y. Han, Z. Zhu and C. Chu, Recent Research Progress of Silicon-Based Anode Materials for Lithium-Ion Batteries, *ChemistrySelect*, 2022, **7**(19), e202201269.
9 W. Ji, H. Qu, X. Zhang, D. Zheng and D. Qu, Electrode Architecture Design to Promote Charge-Transport Kinetics in High-Loading and High-Energy Lithium-Based Batteries, *Small Methods*, 2021, **5**(10), 2100518.
10 H. B. Lin, W. Z. Huang, H. B. Rong, J. N. Hu, S. W. Mai, L. D. Xing, M. Q. Xu, X. P. Li and W. S. Li, Surface natures of conductive carbon materials and their contributions to charge/discharge performance of cathodes for lithium ion batteries, *J. Power Sources*, 2015, **287**, 276–282.
11 T.-W. Kwon, J. W. Choi and A. Coskun, The emerging era of supramolecular polymeric binders in silicon anodes, *Chem. Soc. Rev.*, 2018, 2145–2164.
12 K. Wang, H. Li, X. Chen, Z. Wan, T. Wu, W. Ahmad, D. Qian, X. Wang, J. Gao, R. Khan, M. Ling, D. Yu, J. Chen and C. Liang, Bi-Directional H-Bonding Modulated Soft/Hard Polyethylene Glycol-Polyaniline Coated Si-Anode for High-Performance Li-Ion Batteries, *Small Methods*, 2024, **8**(10), 2301667.
13 J. Shen, S. Zhang, H. Wang, R. Wang, Y. Hu, Y. Mao, R. Wang, H. Zhang, Y. Du, Y. Fan, Y. Zhou, Z. Guo and B. Wang, Unlocking the potential of silicon anodes in lithium-ion batteries: A claw-inspired binder with synergistic interface bonding, *eScience*, 2024, **4**(3), 100207.
14 M. Guo, Z. Cao, Y. Liu, Y. Ni, X. Chen, M. Terrones and Y. Wang, Preparation of Tough, Binder-Free, and Self-Supporting LiFePO4 Cathode by Using Mono-Dispersed Ultra-Long Single-Walled Carbon Nanotubes for High-Rate Performance Li-Ion Battery, *Adv. Sci.*, 2023, **10**(13), 2207355.
15 Y. Shi, L. Wen, S. Pei, M. Wu and F. Li, Choice for graphene as conductive additive for cathode of lithium-ion batteries, *J. Energy Chem.*, 2019, **30**, 19–26.
16 W. Li, M. Li, K. R. Adair, X. Sun and Y. Yu, Carbon nanofiber-based nanostructures for lithium-ion and sodium-ion batteries, *J. Mater. Chem.*, 2017, **5**(27), 13882–13906.
17 B. J. Landi, M. J. Ganter, C. D. Cress, R. A. DiLeo and R. P. Raffaelle, Carbon nanotubes for lithium ion batteries, *Energy Environ. Sci.*, 2009, **2**(6), 638.
18 T. M. Higgins, S.-H. Park, P. J. King, C. Zhang, N. McEvoy, N. C. Berner, D. Daly, A. Shmeliov, U. Khan, G. Duesberg, V. Nicolosi and J. N. Coleman, A Commercial Conducting Polymer as Both Binder and Conductive Additive for Silicon Nanoparticle-Based Lithium-Ion Battery Negative Electrodes, *ACS Nano*, 2016, **10**(3), 3702–3713.
19 L. Huang, Y. You, M. Liu, J. Liu, J. Gu, X. Zhan, W. Wang, F. Wang, H. Tan, S. Wu and L. Zhang, Nanoscale precision welding-enabled quasi-3D conductive carbon blacks for fast-charging and long-lasting secondary batteries, *Carbon*, 2024, **230**, 119688.
20 M. Cao, L. Li, W. Yuan and J. Chen, H_2SO4 etches the surface of Super-P conductive agent: Improving the comprehensive performance of LiNi0.5Co0.2Mn0.3O2 lithium-ion batteries, *Surf. Interfaces*, 2025, **57**, 105789.
21 M. Marinaro, M. Mancini, F. Nobili, R. Tossici, L. Damen and R. Marassi, A newly designed Cu/Super-P composite for the improvement of low-temperature performances of graphite anodes for lithium-ion batteries, *J. Power Sources*, 2013, **222**, 66–71.
22 R. Z. A. Manj, T. Mukhtar, W. U. Rehman, Y. Wang, I. A. Khan, Y. Ma and J. Yang, Unlocking the Role of Covalent Bonding and the Gradient of Hydrogen Bonding in Stabilizing Si-Based Anodes, *ACS Appl. Energy Mater.*, 2025, **8**(12), 7898–7903.
23 J. Li, G. Zeng, S. Horta, P. R. Martínez-Alanis, J. Jacas Biendicho, M. Ibáñez, B. Xu, L. Ci, A. Cabot and Q. Sun, Crystallographic Engineering in Micron-Sized SiOx Anode Material Toward Stable High-Energy-Density Lithium-Ion Batteries, *ACS Nano*, 2025, **19**(16), 16096–16109.
24 Q. Shi, Y. Zhou, J. Cheng, Y. Pan, Y. Wu, L. Zhu and Z. Yuan, Turning carbon black into hollow carbon nanospheres to encapsulate Fe2O3 as high-performance lithium-ion batteries anode, *Microporous Mesoporous Mater.*, 2022, **332**, 111681.
25 X. Qi, B. Blizanac, A. DuPasquier, M. Oljaca, J. Li and M. Winter, Understanding the influence of conductive carbon additives surface area on the rate performance of LiFePO4 cathodes for lithium ion batteries, *Carbon*, 2013, **64**, 334–340.
26 Y. Chen, Y. Ma, Q. Yin, F. Pan, C. Cui, Z. Zhang and B. Liu, Advances in mechanics of hierarchical composite materials, *Compos. Sci. Technol.*, 2021, 108970.
27 Z. Hashin, *Theory of fiber reinforced materials*, 1972.

28 C. Falco, N. Baccile and M.-M. Titirici, Morphological and structural differences between glucose, cellulose and lignocellulosic biomass derived hydrothermal carbons, *Green Chem.*, 2011, 3273.
29 P. Chen, S. Y. Cho and H.-J. Jin, Modification and applications of bacterial celluloses in polymer science, *Macromol. Res.*, 2010, **18**(4), 309–320.
30 C. Rodriguez Correa, T. Hehr, A. Voglhuber-Slavinsky, Y. Rauscher and A. Kruse, Pyrolysis vs. hydrothermal carbonization: Understanding the effect of biomass structural components and inorganic compounds on the char properties, *J. Anal. Appl. Pyrolysis*, 2019, **140**, 137–147.
31 F. Wang, T. Zhang and F. Ran, Bacterial cellulose fiber templated carbonyl-rich dual carbon electrodes for boosting sodium-ion storage, *J. Energy Storage*, 2025, **115**, 115994.
32 M. Hirota, N. Tamura, T. Saito and A. Isogai, Water dispersion of cellulose II nanocrystals prepared by TEMPO-mediated oxidation of mercerized cellulose at pH 4.8, *Cellulose*, 2010, **17**(2), 279–288.
33 Z. Zhou, F. Yu and J. Ma, Nanoconfinement engineering for enchanced adsorption of carbon materials, metal–organic frameworks, mesoporous silica, MXenes and porous organic polymers: a review, *Environ. Chem. Lett.*, 2022, **20**(1), 563–595.
34 S. Afroze and T. K. Sen, A Review on Heavy Metal Ions and Dye Adsorption from Water by Agricultural Solid Waste Adsorbents, *Water, Air, Soil Pollut.*, 2018, **229**(7), 225.
35 J. N. Rouzaud, A. Oberlin and C. Beny-Bassez, Carbon films: Structure and microtexture (optical and electron microscopy, Raman spectroscopy), *Thin Solid Films*, 1983, **105**(1), 75–96.
36 P. Pachfule, D. Shinde, M. Majumder and Q. Xu, Fabrication of carbon nanorods and graphene nanoribbons from a metal–organic framework, *Nat. Chem.*, 2016, 718–724.
37 D. Wu, L. Zhang, J. Zhang, Z. Zhang, F. Liang, L. Jiang, B. Tang, Y. Rui and F. Liu, Novel self-supporting multilevel-3D porous NiO nanowires with metal-organic gel coating via "like dissolves like" to trigger high-performance binder-free lithium-ion batteries, *Microporous Mesoporous Mater.*, 2021, **328**, 111483.
38 Y. Chen, J. Yin, S. Jiang, X. Zhu, Y. Lei, X. Xu and Y. Gao, Poly-1,3-dioxolane anchoring graphitic carbon nitride to achieve high-energy–density solid-state Li metal batteries, *J. Colloid Interface Sci.*, 2023, **652**, 490–499.
39 M. Jiang, H. Luo, J. Chen, L. Chen, W. Jiang and J. Yang, Electrostatic Interactions Dominate the Surface Assembly of Silicon-Based Nanospheres on Carbon Nanofibers for Flexible Lithium-Ion Batteries, *Adv. Funct. Mater.*, 2025, **35**(1), 2411663.
40 T. Young, An Essay on the Cohesion of Fluids, *Philos. Trans. R. Soc. London*, 1805, **95**, 65–87.
41 F. Chen, H. Li, T. Chen, Z. Chen, Y. Zhang, X. Fan, L. Zhan, L. Ma and X. Zhou, Constructing crosslinked lithium polyacrylate/polyvinyl alcohol complex binder for high performance sulfur cathode in lithium-sulfur batteries, *Colloids Surf., A*, 2021, **611**, 125870.
42 G. Che, B. B. Lakshmi, E. R. Fisher and C. R. Martin, Carbon nanotubule membranes for electrochemical energy storage and production, *Nature*, 1998, **393**(6683), 346–349.
43 C. K. Chan, H. Peng, G. Liu, K. McIlwrath, X. F. Zhang, R. A. Huggins and Y. Cui, High-performance lithium battery anodes using silicon nanowires, *Nat. Nanotechnol.*, 2008, 31–35.
44 Z. Cheng, H. Lin, Y. Liu, Q. Yan, B.-L. Su and H. Zhang, A Stress-Buffering Hierarchically Porous Silicon/Carbon Composite for High-Energy Lithium-Ion Batteries, *Adv. Funct. Mater.*, 2025, 2505207.
45 R. Zhang, Z. Xiao, Z. Lin, X. Yan, Z. He, H. Jiang, Z. Yang, X. Jia and F. Wei, Unraveling the Fundamental Mechanism of Interface Conductive Network Influence on the Fast-Charging Performance of SiO-Based Anode for Lithium-Ion Batteries, *Nano-Micro Lett.*, 2023, **16**(1), 43.
46 S. Chen, Z. Deng, J. Li, W. Zhao, B. Nan, Y. Zuo, J. Fang, Y. Huang, Z.-W. Yin, F. Pan and L. Yang, Tuning Reaction Kinetics of Fluorinated Molecules to Construct Robust Solid Electrolyte Interphases on SiO Anode, *Angew. Chem., Int. Ed.*, 2025, **64**(1), e202413927.
47 X. Wang, K. Wang, Z. Wan, Y. Weng, Z. Zheng, J. Zhao, H. Li, D. Qian, Z. Wu, M. Ling and C. Liang, Inorganic/organic composite binder with self-healing property for silicon anode in lithium-ion battery, *Mater. Today Energy*, 2024, **43**, 101567.
48 J. Chen, X. Fan, Q. Li, H. Yang, M. R. Khoshi, Y. Xu, S. Hwang, L. Chen, X. Ji, C. Yang, H. He, C. Wang, E. Garfunkel, D. Su, O. Borodin and C. Wang, Electrolyte design for LiF-rich solid–electrolyte interfaces to enable high-performance microsized alloy anodes for batteries, *Nat. Energy*, 2020, 386–397.
49 W. He, H. Xu, Z. Chen, J. Long, J. Zhang, J. Jiang, H. Dou and X. Zhang, Regulating the Solvation Structure of Li+ Enables Chemical Prelithiation of Silicon-Based Anodes Toward High-Energy Lithium-Ion Batteries, *Nano-Micro Lett.*, 2023, **15**(1), 107.
50 Z. Cheng, H. Lin, Y. Liu, J. Li, H. Jiang and H. Zhang, Enabling the Transport Dynamics and Interfacial Stability of Porous Si Anode Via Rigid and Flexible Carbon Encapsulation for High-Energy Lithium Storage, *Small*, 2024, **20**(52), 2407560.